

Quark and gluon momentum fractions in the pion and in the kaon

Constantia Alexandrou,^{1,2} Simone Bacchio,² Martha Constantinou,³ Joseph Delmar,³
Jacob Finkenrath,⁴ Bartosz Kostrzewa,⁵ Marcus Petschlies,^{6,7} Luis Alberto Rodriguez
Chacon,^{2,8} Gregoris Spanoudes,¹ Fernanda Steffens,^{6,7} Carsten Urbach,^{6,7} and Urs Wenger⁹
(Extended Twisted Mass Collaboration)

¹*Department of Physics, University of Cyprus, Nicosia, Cyprus*

²*Computation-based Science and Technology Research Center, The Cyprus Institute, Nicosia, Cyprus*

³*Department of Physics, Temple University, Philadelphia, PA 19122 - 1801, USA*

⁴*Department of Physics, Bergische Universität Wuppertal, Gaußstraße 20, Wuppertal, 42119, Germany*

⁵*High Performance Computing and Analytics Lab,
Rheinische Friedrich-Wilhelms-Universität Bonn, Germany*

⁶*Helmholtz-Institut für Strahlen- und Kernphysik, University of Bonn, Germany*

⁷*Bethe Center for Theoretical Physics, University of Bonn, Germany*

⁸*University of Ferrara, Ferrara, Italy*

⁹*Institute for Theoretical Physics, Albert Einstein Center for Fundamental Physics, University of Bern, Switzerland*

(Dated: May 15, 2024)

We present the full decomposition of the momentum fraction carried by quarks and gluons in the pion and the kaon. We employ three gauge ensembles generated with $N_f = 2 + 1 + 1$ Wilson twisted-mass clover-improved fermions at the physical quark masses. For both mesons we perform a continuum extrapolation directly at the physical pion mass, which allows us to determine for the first time the momentum decomposition at the physical point. We find that the total momentum fraction carried by quarks is 0.532(56) and 0.618(32) and by gluons 0.388(49) and 0.408(61) in the pion and in the kaon, respectively, in the $\overline{\text{MS}}$ scheme and at the renormalization scale of 2 GeV. Having computed both the quark and gluon contributions in the continuum limit, we find that the momentum sum is 0.926(68) for the pion and 1.046(90) for the kaon, verifying the momentum sum rule.

Introduction — Quantum Chromodynamics (QCD) governs the formation of hadron bound states through the interaction of quarks and gluons. Understanding how these constituents combine to define the observable properties of hadrons has been the subject of extensive research spanning the last six decades. Among the diverse spectrum of hadrons, the light pseudo-scalar mesons hold a special place, as they encapsulate a key property of the QCD dynamics: they are recognized as pseudo-Goldstone bosons arising from the spontaneous breaking of chiral symmetry in QCD, characterized by their significantly smaller masses when compared to the more abundant nucleons. In addition, they stand out for their valence quark-antiquark composition, in contrast to the structure of three valence quarks in the nucleons. This inner structure is mostly studied through the use of parton distribution functions (PDFs), which measure, in the simplest case of unpolarized hadrons, the probability of a parton to carry a fraction x of the hadron momentum. As a result, PDFs and their averages, the so-called first moment of the PDFs, are essential quantities to pin down the structure of any hadron.

Among the pseudo-Goldstone bosons, pions and kaons are the simplest and the lightest. And while pions are comprised of valence up and down quarks and antiquarks, kaons are formed by combining either an up

or a down quark (antiquark) with a strange antiquark (quark). Thus, a significant distinguishing feature between pions and kaons lies in the mass of the strange quark, the mass of which exceeds the sum of the masses of the two light quarks by more than twenty fold, while the pion mass is approximately one-fourth of the kaon mass. Moreover, in the chiral limit their masses vanish, while the mass of the nucleon is significantly less affected. We may then say that comprehending the pion and the kaon structures, their similarities and differences, allows us to gain a deeper understanding of QCD itself, possibly providing hints on the nonperturbative mechanisms behind the generation of hadron masses. Indeed, the future Electron-Ion Collider (EIC) [1–3] has among its aims to increase our knowledge of the partonic structure of pions and kaons, and to quantify what are the quark and gluon energy contributions to the mass of pions and kaons.

Experimental data for the pion PDFs and their moments is scarce, restricted to limited data from several decades ago, when they were measured in pion-induced Drell-Yan processes [4]. For the kaon, the situation is even worse, with only a handful of data [5]. These early data has been included in modern global analysis [6–10] and used to determine the pion PDFs, while the kaon distributions have been studied mostly within models [11–18]. On the theory side, lattice QCD can investigate the

partonic structure of hadrons either through the direct computation of the PDFs [19] or through their moments, employing the method of local operators. Based on this latter method, the body of lattice QCD studies on the pion structure remains relatively modest in comparison to those focused on the nucleon, a situation that is more pronounced when considering studies on the structure of kaons. Many of the existing studies for the pion case either omit disconnected diagrams [20–26] or only incorporate a partial portion of the disconnected contributions [27]. The only exceptions are [28, 29]. In our previous work [28], we performed the first comprehensive breakdown of the pion momentum into its constituent quark and gluon components. The authors of [29] also presented a full momentum decomposition, albeit at larger than physical pion mass and at a single lattice spacing. While our previous work was conducted at the physical pion mass, it was also restricted to a single lattice spacing. In Ref. [30], an extrapolation to the continuum is made, but using ensembles generated with heavier-than-physical pion masses. Moreover, their result is restricted to the gluons only. In the case of the kaon, there is one previous study [26], where only connected contributions are considered and again a heavier than physical pion mass is used. Going beyond the use of local operators, the last few years witnessed the development of a variety of new methods [19], based on nonlocal operators, which allow us to access the whole Bjorken x dependence of PDFs. In particular, the x dependence of PDFs for pions and kaons has been computed within the quasi-PDF [31–34] and the pseudo-PDF [35, 36] approaches, as well as in the so called “good lattice cross sections” method involving hadronic matrix elements computed on the lattice that are constructed to be time independent [37, 38]. Nevertheless, these works are restricted to the valence quark distributions, with the exception of [36] where only the gluon distribution is computed using ensembles with heavier than physical pion masses. It is clear from this discussion that the full momentum decomposition of the pion and of the kaon is needed, both at the physical pion mass and with an extrapolation to the continuum. Therefore, in this work we perform the first momentum decomposition of both pions and kaons using a lattice QCD computation at the physical point.

Lattice Setup — The parameters of the gauge field ensembles of the Extended Twisted Mass Collaboration (ETMC) used in this work are listed in Table I, with the corresponding lattice spacing, lattice size and two most relevant hadron masses for charged pion and kaon. All ensembles have $N_f = 2 + 1 + 1$ quarks, with masses of up, down, strange and charm quark tuned to reproduce the physical pion mass, as well as the physical value of the ratios M_{D_s}/f_{D_s} and m_c/m_s , see Ref. [39] for details. We extract the momentum fractions carried by the partons from the matrix elements of the energy-momentum

TABLE I. ETMC ensembles analyzed. a is the lattice spacing and $L(T = 2L)$ the lattice spatial (temporal) extent in fm, and M_{π^\pm} and M_{K^\pm} the charged pion and kaon mass, respectively.

Ensemble	a [fm]	L [fm]	M_{π^\pm} [MeV]	M_{K^\pm} [MeV]
cB211.072.64 (B)	0.0796(1)	5.09	140.40(22)	498.41(11)
cC211.060.80 (C)	0.0682(1)	5.46	136.05(30)	495.27(14)
cD211.054.96 (D)	0.0569(1)	5.46	141.01(22)	494.77(11)

tensor (EMT),

$$\langle h(\mathbf{p}) | \bar{T}_{\mu\nu}^X | h(\mathbf{p}) \rangle = 2\langle x \rangle_X \left(p_\mu p_\nu - \delta_{\mu\nu} \frac{p^2}{4} \right) \quad (1)$$

where $h(\mathbf{p})$ denotes a hadron state with mass m_h , and $p = (E_h(\mathbf{p}), \mathbf{p})$ the on-shell four-momentum, with $E_h(\mathbf{p}) = \sqrt{m_h^2 + \mathbf{p}^2}$. The index $X = q, g$ denotes the contributions from individual quark flavors ($q = u, d, s, c$) and gluons to the hadron momentum. We compute the matrix elements appearing on the left-hand side of Eq. (1) through the ratio of three- and two-point functions

$$R_{\mu\nu}^X(t_{\text{ins}}, t_s; \mathbf{p}) = \frac{\langle h(t_s, \mathbf{p}) | \bar{T}_{\mu\nu}^X(t_{\text{ins}}) | h(0, \mathbf{p}) \rangle}{\langle h(t_s, \mathbf{p}) | h(0, \mathbf{p}) \rangle}. \quad (2)$$

If t_s and $t_s - t_{\text{ins}}$ are large enough, then asymptotically up to contamination by excited states above the ground state $|h(\mathbf{p})\rangle$

$$R_{\mu\nu}^X(t, t_f, t_i; \mathbf{p}) \rightarrow \frac{1}{2E_h} \frac{\langle h(\mathbf{p}) | \bar{T}_{\mu\nu}^X | h(\mathbf{p}) \rangle}{1 + \exp(-E_h(T - 2t_s))}. \quad (3)$$

The quark part of the EMT is given by

$$\bar{T}_{\mu\nu}^q = -\frac{(i)^{\kappa_{\mu\nu}}}{4} \bar{q} \left(\gamma_\mu \overleftrightarrow{D}_\nu + \gamma_\nu \overleftrightarrow{D}_\mu - \delta_{\mu\nu} \frac{1}{2} \gamma_\rho \overleftrightarrow{D}_\rho \right) q, \quad (4)$$

with $\kappa_{\mu\nu} = \delta_{\mu,4} \delta_{\nu,4}$, and $\overleftrightarrow{D}_\mu$ the symmetrized covariant derivative. The gluon EMT is given through the gluon field-strength tensor $F_{\mu\nu}$ by

$$\bar{T}_{\mu\nu}^g = (i)^{\kappa_{\mu\nu}} \left(F_{\mu\rho} F_{\nu\rho} + F_{\nu\rho} F_{\mu\rho} - \delta_{\mu\nu} \frac{1}{2} F_{\rho\sigma} F_{\rho\sigma} \right). \quad (5)$$

We note that both expressions have been written for a Euclidean space-time. While quark-connected and -disconnected diagrams contribute to the 3-point functions with quark EMT insertion, the gluonic EMT insertion produces only purely disconnected diagrams (cf. Fig. 10 in the Supplementary Material I).

Bare momentum fractions — Equation (3), combined with Eq. (1), allows us to determine $\langle x \rangle$ from different components of the EMT. We compute the connected contributions using the tensor element \bar{T}_{44} with hadron momentum $\mathbf{p} = 0$, while for the disconnected contributions we employ the combination of components \bar{T}_{4k} ,

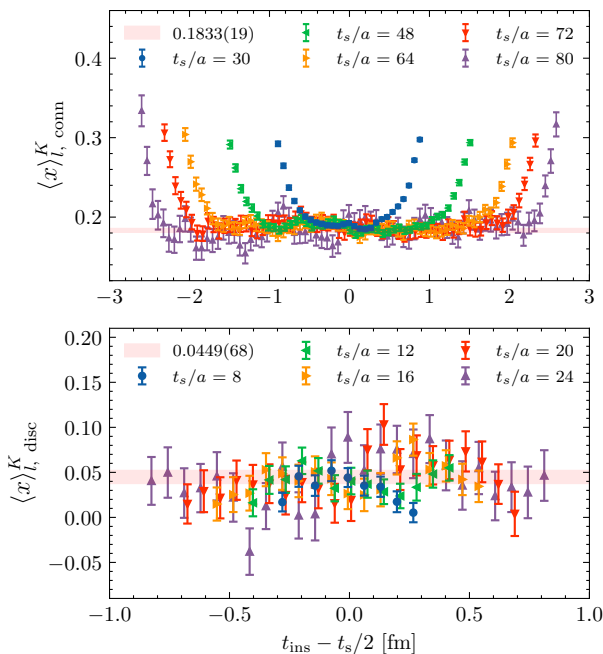


FIG. 1. Bare ratios of the light-quark momentum fraction in the kaon dependence on the sink-source time separation t_s for the C ensemble. In the upper panel, we show the ratio for the connected contribution and in the lower panel, the ratio for the disconnected contribution. We show results for several values of t_s , from $t_s/a = 30$ to $t_s/a = 80$. The red bands show the result after model averaging of fits to a constant when varying the ranges of t_s used.

$k = 1, 2, 3$, with nonzero momentum $|\mathbf{p}| = 2\pi/L$. We thereby optimize the signal-to-noise ratio for each type of contribution: the temporal-spatial EMT elements \bar{T}_{4k} do not require additive renormalization by trace subtraction and with minimal nonzero hadron momentum allow for most precise projection on the hadron ground state, necessary for the weak signal in the disconnected diagrams. On the other hand, statistical noise from trace subtraction is negligible for the connected diagrams from \bar{T}_{44} , while zero hadron momentum renders the ground state projection most precise. By Eq. (1) and Lorentz-covariance, the matrix elements from different tensor components become equivalent in the continuum limit. As an illustration of the data, we show the ratios for connected and disconnected contributions for the light quarks in the kaon in Fig. 1 for the ensemble C in Table I. The ratios were computed for several source-sink separations t_s , and we see in Fig. 1 the formation of a plateau for large values of t_s . We fitted the plateau using different combinations of t_s and of the insertion time t_{ins} . Model averaging [40] is used on the results from the plateau fit in order to obtain $\langle x \rangle$. The same procedure is employed for the ratios involving the gluon EMT insertion. To optimize the signal-to-noise ratio we apply four-dimensional stout smearing [41] to the gauge field in the lattice gluon field-strength tensor when constructing

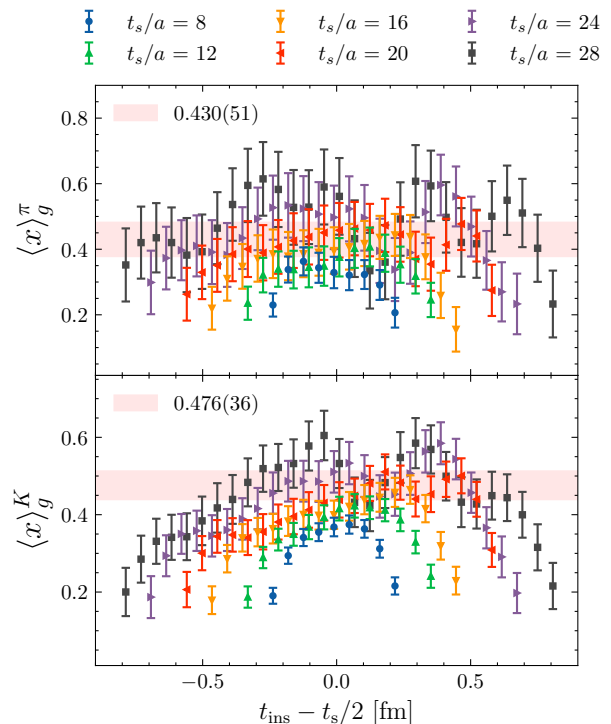


FIG. 2. Examples of the bare ratios for the gluon contribution, for six values of the time sink-source separation t_s using 10 stout-smearing steps. The top panel shows the pion and the bottom panel the kaon case. The horizontal bands show the model-averaged fit results.

\bar{T}_{4k}^g . In Fig. 2 we show the ratio for several values of t_s for $N_{\text{stout}} = 10$ smearing steps, for both pion and kaon case.

We probe the systematic dependence on the level of stout smearing by comparing the average momentum fraction for the range of stout-smearing steps $5 \leq N_{\text{stout}} \leq 10$, weighted by the renormalization factor Z_{gg} , which is determined for the corresponding values of N_{stout} . As we find agreement among those individual results, we then perform a simultaneous fit to the Z_{gg} -weighted ratios from this set of stout-smearing steps. All the plateau fits, as well as the results after model averaging, for each ensemble and flavor, are shown in the Supplemental Material I.

Renormalization and continuum limit — We proceed with the renormalization procedure for the flavor-singlet and flavor-nonsinglet combinations. The renormalized results are given in the $\overline{\text{MS}}$ scheme at scale 2 GeV. The flavor-nonsinglet combinations are renormalized with the nonperturbatively determined renormalization factor Z_{qq} as

$$\begin{aligned} \langle x \rangle_{u+d-2s,R} &= Z_{qq}(\langle x \rangle_u + \langle x \rangle_d - 2\langle x \rangle_s), \\ \langle x \rangle_{u+d+s-3c,R} &= Z_{qq}(\langle x \rangle_u + \langle x \rangle_d + \langle x \rangle_s - 3\langle x \rangle_c). \end{aligned} \quad (6)$$

Compared to our previous analysis [28], we now use

$\mathcal{O}(\alpha_s^4)$ corrections to the anomalous dimension, thus improving the scale evolution of the data to the common 2 GeV scale used throughout this work. The quark-singlet and gluon components mix under renormalization according to

$$\begin{pmatrix} \langle x \rangle_{q,R} \\ \langle x \rangle_{g,R} \end{pmatrix} = \begin{pmatrix} Z_{qq}^s & Z_{qg} \\ Z_{gq} & Z_{gg} \end{pmatrix} \begin{pmatrix} \langle x \rangle_q \\ \langle x \rangle_g \end{pmatrix} \quad (7)$$

with Z_{qq}^s the quark-singlet renormalization constant and the total bare (renormalized) quark contribution is denoted by

$$\langle x \rangle_{q,(R)} = \sum_{f=u,d,s,c} \langle x \rangle_{f,(R)}. \quad (8)$$

Defining $\delta Z_{qq} = Z_{qq}^s - Z_{qq}$, one can solve Eq. (7) for each single flavor and the gluon component:

$$\begin{aligned} \langle x \rangle_{f,R} &= Z_{qq} \langle x \rangle_f + \frac{\delta Z_{qq}}{N_f} \sum_{f'} \langle x \rangle_{f'} + \frac{Z_{qg}}{N_f} \langle x \rangle_g, \\ \langle x \rangle_{g,R} &= Z_{gg} \langle x \rangle_g + Z_{gq} \sum_{f'} \langle x \rangle_{f'}. \end{aligned} \quad (9)$$

The calculation of Z_{gq} and Z_{gg} have also been improved, with the details presented in the Supplemental Material. For the twisted-mass lattice action at maximal twist with automatic $\mathcal{O}(a)$ improvement we expect leading discretization artefacts at second order in the lattice spacing a . We, thus, take the continuum limit using a constant or a linear fit in a^2 , for both the renormalized quark and gluon contributions, for the pion and the kaon cases. Our final value is the result of the model average among these fits. In Fig. (3), we show the linear extrapolation of the total renormalized quark contribution $\langle x \rangle_{q,R}$, the gluon contribution $\langle x \rangle_{g,R}$, and in addition their sum. We note that the total quark contribution to $\langle x \rangle^K$ tends to be higher than its analog in the pion, as also observed in Ref [14]. The gluon contribution to the pion and to the kaon momenta, however, are compatible within errors, and the momentum sum rule

$$\langle x \rangle_{q,R} + \langle x \rangle_{g,R} = 1 \quad (10)$$

is satisfied, in both cases, within a standard deviation. The full list of the renormalized results in the continuum limit, for both pion and kaon, is presented in Table II at the scale of $\mu = 2$ GeV in the $\overline{\text{MS}}$ scheme.

In Fig. 4, we show a comparison of our results with those from other groups. We include recent results from phenomenological analyses [7, 8], from the Dyson Schwinger equations (DSE) [14], from a calculation using the light-front wave function (LFWF) approach [15] and from lattice QCD computations [27, 30], limiting ourselves to those which are extrapolated to the physical pion mass and/or the continuum limit. The lattice QCD results shown are computed using ensembles simulated with pion masses larger than physical and then

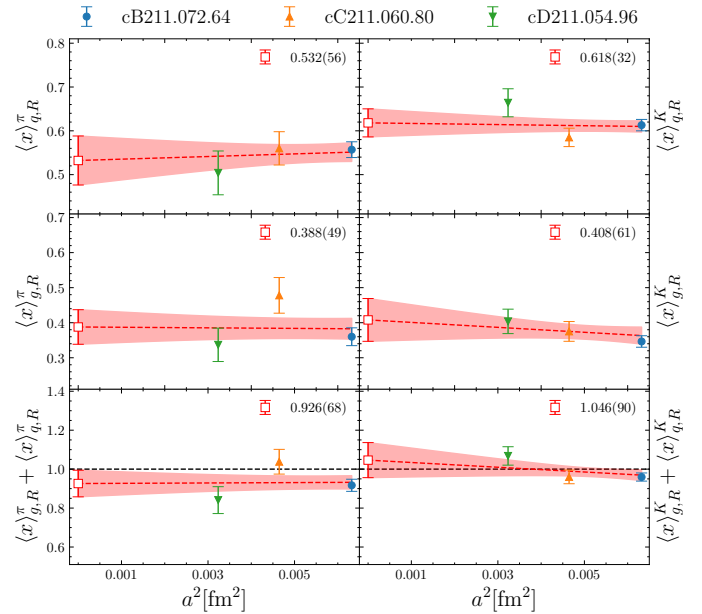


FIG. 3. Continuum limit extrapolation for the pion (left panel) and the kaon (right panel). We present our results for the total quark and gluon contributions, as well as the momentum sum rule. The blue filled circles are results for ensemble B [28], the orange upwards triangles for ensemble C and the green downwards triangles for ensemble D. The open symbol is the result after model averaging between constant and linear fit. Further details can be found in the Supplemental Material.

extrapolated to the physical pion mass. Furthermore, they both considered only a partial sum of disconnected contributions, namely only the quark disconnected is considered in Ref. [27] but not the gluon contribution, whereas only the gluon is considered in Ref. [30]. For the cases where all contributions are included, the data is restricted to only one lattice spacing [28] at physical pion mass or using larger than physical pion masses [26, 29]. Our result for $\langle x \rangle_{g,R}^{\pi}$ is in agreement with the one from Ref. [30] as is our result for $\langle x \rangle_{q,R}^{\pi}$ with RQCD [27] that carries however a large error. Compared to our previous work [28] using only the B ensemble, taking the continuum extrapolation increases the error, as can be seen in Fig. 3. For the kaon, the only available lattice QCD data [26] is for one lattice spacing using an ensemble with a heavier-than-physical pion mass and thus one cannot directly compare to the present work.

Conclusions and outlook — We present in this work the first complete momentum decomposition for both the pion and the kaon in terms of their quark and gluon constituents, performed within lattice QCD at the physical point. Three ensembles with $N_f = 2 + 1 + 1$ quark flavors with their masses tuned to reproduce the physical light, strange and charm quark masses are analyzed. We use a model average for the continuum extrapolation

TABLE II. Compilation of results for the pion and for the kaon in the continuum limit. All quantities are presented at the scale 2 GeV in the $\overline{\text{MS}}$ scheme.

	π	K
$\langle x \rangle_{l,R}$	0.448(34)	0.260(09)
$\langle x \rangle_{s,R}$	0.043(15)	0.333(11)
$\langle x \rangle_{c,R}$	0.019(17)	0.024(17)
$\langle x \rangle_{g,R}$	0.388(49)	0.408(61)
$\langle x \rangle_{q,R}$	0.532(56)	0.618(32)
$\langle x \rangle_{u+d-2s,R}$	0.382(17)	-0.409(16)
$\langle x \rangle_{u+d+s-3c,R}$	0.445(48)	0.487(39)

performed using both a constant and a linear fit in the squared lattice spacing, a^2 . Our results for $\langle x \rangle_g^{\pi,K}$ indicate a similar momentum fraction carried by gluons in the kaon and the pion. However, they have larger errors than the corresponding quark momentum fraction $\langle x \rangle_q^{\pi,K}$, which tends to be smaller in the pion. This indicates a possible larger momentum fraction carried by gluons in the pion as compared to the kaon. Thus, among possible improvements, in future work both the statistical and systematic errors, in particular for $\langle x \rangle_g$, will be reduced. This can be accomplished by increasing the number of gauge configurations and source positions used for the two-point functions, Eq. (3), improving the statistical accuracy in the determination of the gluon momentum fraction. In addition, we plan to analyze an additional ensemble closer to the continuum limit in order to help a better error control when performing the continuum extrapolation. However, the current work presents a remarkable achievement as we now have a fully consistent theoretical calculation that allows us to directly compare the pion and the kaon at the level of their quark and gluon structure. In particular, the momentum sum rule can be tested by computing all components from first principles. We stress that prior to the current work, there was no such decomposition into quark and gluon parts available of $\langle x \rangle^K$ using a first-principles calculation. Furthermore, the current work demonstrates clearly that the momentum fraction carried by gluons and sea quarks (the disconnected contributions) are important components of the two lightest pseudo-Goldstone bosons, and added together with the valence contributions verify the momentum sum rule for both cases.

ACKNOWLEDGMENTS

G.S. acknowledges financial support from the European Regional Development Fund and the Republic of Cyprus through the Cyprus Research and Innovation Foundation under contract number EXCELLENCE/0421/0195. This project is partly funded by the European Union's Horizon 2020 Research and Innovation Programme ENGAGE under the Marie Skłodowska-Curie COFUND scheme with grant agreement No. 101034267. C.A. acknowledges partial support from the European Regional Development

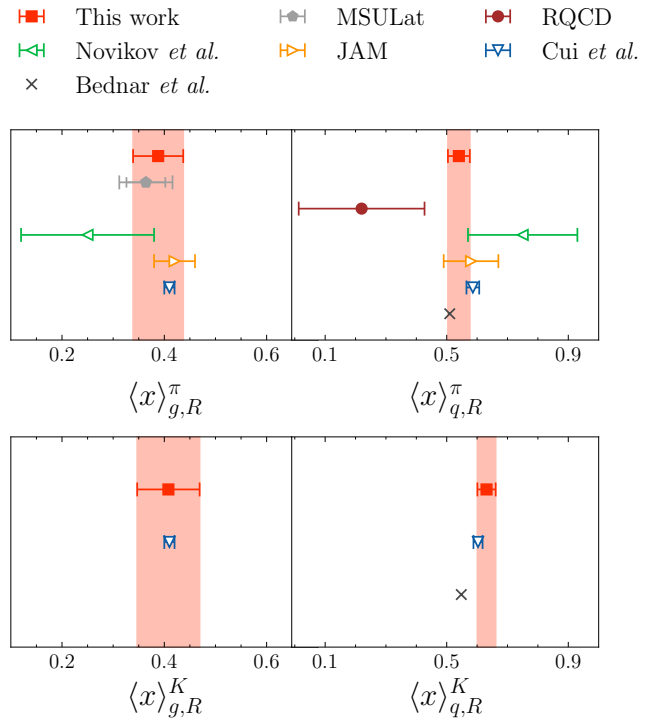


FIG. 4. Comparison of the results of this work, with other available data, both from phenomenology and from lattice QCD. All results are given in the $\overline{\text{MS}}$ scheme at the scale of $\mu = 2$ GeV. The upper panels show the results for the pion gluon (left) and quark (right) momentum fractions, $\langle x \rangle_{g,R}^{\pi}$ and $\langle x \rangle_{q,R}^{\pi}$, respectively. The lower panels show the corresponding results for the kaon. The red filled squares show the results of this work with the red band the associated error band. Recent results from phenomenological analyses of PDFs data are given by open symbols: left green triangle (Novikov *et al.* [7]) and right orange triangle (JAM Collaboration [8]). The result while the result based on the LFWF is represented by the down blue triangle (Cui *et al.* [15]), while using the DSE [14] by the black cross, where no error is provided. Recent lattice QCD results extrapolated to the continuum limit are given by the brown filled circle (RQCD [27]) and the gray pentagon (MSULat [30]).

Fund and the Republic of Cyprus through the Cyprus Research and Innovation Foundation under contract number EXCELLENCE/0421/0043 and the European Joint Doctorate project AQTIVATE funded by the European Commission under the Marie Skłodowska-Curie Doctoral Networks action and Grant Agreement No 101072344. This work is supported by the Swiss National Science Foundation (SNSF) through grant No. 200021_175761, 200021_208222, and 200020_200424, as well as by the DFG and the NFSC as part of the Sino-German Collaborative Research Center CRC110 “Symmetries and the emergence of structure”. J. D. and M. C. acknowledge financial support from the U.S. Department of Energy, Office of Nuclear Physics, Early Career Award under Grant No. DE-SC0020405. We gratefully acknowledge computing time granted on Piz Daint at Centro

Svizzero di Calcolo Scientifico (CSCS) via the projects s849, s982, s1045, s1133 and s1197 and the Gauss Centre for Supercomputing e.V. (www.gauss-centre.eu) for funding this project by providing computing time on the GCS Supercomputers SuperMUC-NG at Leibniz Supercomputing Centre and JUWELS [42] at Juelich Supercomputing Centre. The authors acknowledge the Texas Advanced Computing Center (TACC) at The University of Texas at Austin for providing HPC resources (Project ID PHY21001). J.F. is supported by the DFG research unit FOR5269 "Future methods for studying confined gluons in QCD". The authors gratefully acknowledge PRACE for awarding access to HAWK at HLRS within the project with Id Acid 4886, and the

Swiss National Supercomputing Centre (CSCS) and the EuroHPC Joint Undertaking for awarding this project access to the LUMI supercomputer, owned by the EuroHPC Joint Undertaking, hosted by CSC (Finland) and the LUMI consortium through the Chronos programme under project IDs CH17-CSCS-CYP and CH21-CSCS-UNIBE as well as the EuroHPC Regular Access Mode under project ID EHPC-REG-2021R0095. The open source software packages tmLQCD [43–45], Lemon [46], QUDA [47–49], R [50], cvc [51] and plegma have been used. Finally, We thank the authors of [15] and [14] for kindly sending us their results evolved to the scale used in our computation, 2 GeV.

-
- [1] Arlene C. Aguilar *et al.*, "Pion and Kaon Structure at the Electron-Ion Collider," *Eur. Phys. J. A* **55**, 190 (2019), [arXiv:1907.08218 \[nucl-ex\]](https://arxiv.org/abs/1907.08218).
- [2] R. Abdul Khalek *et al.*, "Science Requirements and Detector Concepts for the Electron-Ion Collider: EIC Yellow Report," *Nucl. Phys. A* **1026**, 122447 (2022), [arXiv:2103.05419 \[physics.ins-det\]](https://arxiv.org/abs/2103.05419).
- [3] Gang Xie, Chengdong Han, Rong Wang, and Xurong Chen, "Tackling the kaon structure function at EicC *," *Chin. Phys. C* **46**, 064107 (2022), [arXiv:2109.08483 \[hep-ph\]](https://arxiv.org/abs/2109.08483).
- [4] J. S. Conway *et al.*, "Experimental Study of Muon Pairs Produced by 252-GeV Pions on Tungsten," *Phys. Rev. D* **39**, 92–122 (1989).
- [5] J. Badier *et al.* (Saclay-CERN-College de France-Ecole Poly-Orsay), "Measurement of the K^-/π^- Structure Function Ratio Using the Drell-Yan Process," *Phys. Lett. B* **93**, 354–356 (1980).
- [6] P. C. Barry, N. Sato, W. Melnitchouk, and Chueng-Ryong Ji, "First Monte Carlo Global QCD Analysis of Pion Parton Distributions," *Phys. Rev. Lett.* **121**, 152001 (2018), [arXiv:1804.01965 \[hep-ph\]](https://arxiv.org/abs/1804.01965).
- [7] Ivan Novikov *et al.*, "Parton Distribution Functions of the Charged Pion Within The xFitter Framework," *Phys. Rev. D* **102**, 014040 (2020), [arXiv:2002.02902 \[hep-ph\]](https://arxiv.org/abs/2002.02902).
- [8] P. C. Barry, Chueng-Ryong Ji, N. Sato, and W. Melnitchouk (Jefferson Lab Angular Momentum (JAM)), "Global QCD Analysis of Pion Parton Distributions with Threshold Resummation," *Phys. Rev. Lett.* **127**, 232001 (2021), [arXiv:2108.05822 \[hep-ph\]](https://arxiv.org/abs/2108.05822).
- [9] P. C. Barry *et al.* (Jefferson Lab Angular Momentum (JAM), HadStruc), "Complementarity of experimental and lattice QCD data on pion parton distributions," *Phys. Rev. D* **105**, 114051 (2022), [arXiv:2204.00543 \[hep-ph\]](https://arxiv.org/abs/2204.00543).
- [10] Lucas Kotz, Aurore Courtoy, Pavel Nadolsky, Fredrick Olness, and Maximiliano Ponce-Chavez, "An analysis of parton distributions in a pion with Bézier parametrizations," (2023), [arXiv:2311.08447 \[hep-ph\]](https://arxiv.org/abs/2311.08447).
- [11] Chen Chen, Lei Chang, Craig D. Roberts, Shaolong Wan, and Hong-Shi Zong, "Valence-quark distribution functions in the kaon and pion," *Phys. Rev. D* **93**, 074021 (2016), [arXiv:1602.01502 \[nucl-th\]](https://arxiv.org/abs/1602.01502).
- [12] Chao Shi, Cédric Mezrag, and Hong-shi Zong, "Pion and kaon valence quark distribution functions from Dyson-Schwinger equations," *Phys. Rev. D* **98**, 054029 (2018), [arXiv:1806.10232 \[nucl-th\]](https://arxiv.org/abs/1806.10232).
- [13] Jiangshan Lan, Chandan Mondal, Shaoyang Jia, Xingbo Zhao, and James P. Vary, "Pion and kaon parton distribution functions from basis light front quantization and QCD evolution," *Phys. Rev. D* **101**, 034024 (2020), [arXiv:1907.01509 \[nucl-th\]](https://arxiv.org/abs/1907.01509).
- [14] Kyle D. Bednar, Ian C. Cloët, and Peter C. Tandy, "Distinguishing Quarks and Gluons in Pion and Kaon Parton Distribution Functions," *Phys. Rev. Lett.* **124**, 042002 (2020), [arXiv:1811.12310 \[nucl-th\]](https://arxiv.org/abs/1811.12310).
- [15] Zhu-Fang Cui, Minghui Ding, Fei Gao, Khépani Raya, Daniele Binosi, Lei Chang, Craig D Roberts, Jose Rodríguez-Quintero, and Sebastian M Schmidt, "Kaon and pion parton distributions," *Eur. Phys. J. C* **80**, 1064 (2020).
- [16] Chengdong Han, Gang Xie, Rong Wang, and Xurong Chen, "An Analysis of Parton Distribution Functions of the Pion and the Kaon with the Maximum Entropy Input," *Eur. Phys. J. C* **81**, 302 (2021), [arXiv:2010.14284 \[hep-ph\]](https://arxiv.org/abs/2010.14284).
- [17] Craig D. Roberts, David G. Richards, Tanja Horn, and Lei Chang, "Insights into the emergence of mass from studies of pion and kaon structure," *Prog. Part. Nucl. Phys.* **120**, 103883 (2021), [arXiv:2102.01765 \[hep-ph\]](https://arxiv.org/abs/2102.01765).
- [18] Barbara Pasquini, Simone Rodini, and Simone Venturini (MAP (Multi-dimensional Analyses of Partonic distributions)), "Valence quark, sea, and gluon content of the pion from the parton distribution functions and the electromagnetic form factor," *Phys. Rev. D* **107**, 114023 (2023), [arXiv:2303.01789 \[hep-ph\]](https://arxiv.org/abs/2303.01789).
- [19] Martha Constantinou, "The x-dependence of hadronic parton distributions: A review on the progress of lattice QCD," *Eur. Phys. J. A* **57**, 77 (2021), [arXiv:2010.02445 \[hep-lat\]](https://arxiv.org/abs/2010.02445).
- [20] G. Martinelli and Christopher T. Sachrajda, "Pion Structure Functions From Lattice QCD," *Phys. Lett. B* **196**, 184–190 (1987).
- [21] C. Best, M. Göckeler, R. Horsley, Ernst-Michael Ilgenfritz, H. Perlt, Paul E. L. Rakow, A. Schäfer, G. Schierholz, A. Schiller, and S. Schramm, "Pion and rho structure functions from lattice QCD," *Phys. Rev. D* **56**, 2743–2754 (1997), [arXiv:hep-lat/9703014](https://arxiv.org/abs/hep-lat/9703014).

- [22] M. Guagnelli, K. Jansen, F. Palombi, R. Petronzio, A. Shindler, and I. Wetzorke (Zeuthen-Rome (ZeRo)), “Non-perturbative pion matrix element of a twist-2 operator from the lattice,” *Eur. Phys. J. C* **40**, 69–80 (2005), [arXiv:hep-lat/0405027](#).
- [23] S. Capitani, K. Jansen, M. Papinutto, A. Shindler, C. Urbach, and I. Wetzorke, “Parton distribution functions with twisted mass fermions,” *Phys. Lett. B* **639**, 520–526 (2006), [arXiv:hep-lat/0511013](#).
- [24] A. Abdel-Rehim *et al.*, “Nucleon and pion structure with lattice QCD simulations at physical value of the pion mass,” *Phys. Rev. D* **92**, 114513 (2015), [Erratum: *Phys.Rev.D* 93, 039904 (2016)], [arXiv:1507.04936 \[hep-lat\]](#).
- [25] M. Oehm, C. Alexandrou, M. Constantinou, K. Jansen, G. Koutsou, B. Kostrzewa, F. Steffens, C. Urbach, and S. Zafeiropoulos, “ $\langle x \rangle$ and $\langle x^2 \rangle$ of the pion PDF from lattice QCD with $N_f = 2+1+1$ dynamical quark flavors,” *Phys. Rev. D* **99**, 014508 (2019), [arXiv:1810.09743 \[hep-lat\]](#).
- [26] Constantia Alexandrou, Simone Bacchio, Ian Cloet, Martha Constantinou, Kyriakos Hadjiyiannakou, Giannis Koutsou, and Colin Lauer (ETM), “Mellin moments $\langle x \rangle$ and $\langle x^2 \rangle$ for the pion and kaon from lattice QCD,” *Phys. Rev. D* **103**, 014508 (2021), [arXiv:2010.03495 \[hep-lat\]](#).
- [27] Marius Löffler, Philipp Wein, Thomas Wurm, Simon Weishäupl, Daniel Jenkins, Rudolf Rödl, Andreas Schäfer, and Lisa Walter (RQCD), “Mellin moments of spin dependent and independent PDFs of the pion and rho meson,” *Phys. Rev. D* **105**, 014505 (2022), [arXiv:2108.07544 \[hep-lat\]](#).
- [28] Constantia Alexandrou *et al.* (Extended Twisted Mass), “Quark and Gluon Momentum Fractions in the Pion from $N_f=2+1+1$ Lattice QCD,” *Phys. Rev. Lett.* **127**, 252001 (2021), [arXiv:2109.10692 \[hep-lat\]](#).
- [29] Daniel C. Hackett, Patrick R. Oare, Dimitra A. Pefkou, and Phiala E. Shanahan, “Gravitational form factors of the pion from lattice QCD,” (2023), [arXiv:2307.11707 \[hep-lat\]](#).
- [30] William Good, Kinza Hasan, Allison Chevis, and Huey-Wen Lin, “The Gluon Moment and Parton Distribution Function of the Pion from $N_f = 2 + 1 + 1$ Lattice QCD,” (2023), [arXiv:2310.12034 \[hep-lat\]](#).
- [31] Jian-Hui Zhang, Jiunn-Wei Chen, Luchang Jin, Huey-Wen Lin, Andreas Schäfer, and Yong Zhao, “First direct lattice-QCD calculation of the x -dependence of the pion parton distribution function,” *Phys. Rev. D* **100**, 034505 (2019), [arXiv:1804.01483 \[hep-lat\]](#).
- [32] Taku Izubuchi, Luchang Jin, Christos Kallidonis, Nikhil Karthik, Swagato Mukherjee, Peter Petreczky, Charles Shugert, and Sergey Syritsyn, “Valence parton distribution function of pion from fine lattice,” *Phys. Rev. D* **100**, 034516 (2019), [arXiv:1905.06349 \[hep-lat\]](#).
- [33] Huey-Wen Lin, Jiunn-Wei Chen, Zhouyou Fan, Jian-Hui Zhang, and Rui Zhang, “Valence-Quark Distribution of the Kaon and Pion from Lattice QCD,” *Phys. Rev. D* **103**, 014516 (2021), [arXiv:2003.14128 \[hep-lat\]](#).
- [34] Xiang Gao, Luchang Jin, Christos Kallidonis, Nikhil Karthik, Swagato Mukherjee, Peter Petreczky, Charles Shugert, Sergey Syritsyn, and Yong Zhao, “Valence parton distribution of the pion from lattice QCD: Approaching the continuum limit,” *Phys. Rev. D* **102**, 094513 (2020), [arXiv:2007.06590 \[hep-lat\]](#).
- [35] Bálint Joó, Joseph Karpie, Kostas Orginos, Anatoly V. Radyushkin, David G. Richards, Raza Sabbir Sufian, and Savvas Zafeiropoulos, “Pion valence structure from Ioffe-time parton pseudodistribution functions,” *Phys. Rev. D* **100**, 114512 (2019), [arXiv:1909.08517 \[hep-lat\]](#).
- [36] Alejandro Salas-Chavira, Zhouyou Fan, and Huey-Wen Lin, “First glimpse into the kaon gluon parton distribution using lattice QCD,” *Phys. Rev. D* **106**, 094510 (2022), [arXiv:2112.03124 \[hep-lat\]](#).
- [37] Raza Sabbir Sufian, Joseph Karpie, Colin Egerer, Kostas Orginos, Jian-Wei Qiu, and David G. Richards, “Pion Valence Quark Distribution from Matrix Element Calculated in Lattice QCD,” *Phys. Rev. D* **99**, 074507 (2019), [arXiv:1901.03921 \[hep-lat\]](#).
- [38] Raza Sabbir Sufian, Colin Egerer, Joseph Karpie, Robert G. Edwards, Bálint Joó, Yan-Qing Ma, Kostas Orginos, Jian-Wei Qiu, and David G. Richards, “Pion Valence Quark Distribution from Current-Current Correlation in Lattice QCD,” *Phys. Rev. D* **102**, 054508 (2020), [arXiv:2001.04960 \[hep-lat\]](#).
- [39] Constantia Alexandrou *et al.*, “Simulating twisted mass fermions at physical light, strange and charm quark masses,” *Phys. Rev. D* **98**, 054518 (2018), [arXiv:1807.00495 \[hep-lat\]](#).
- [40] William I. Jay and Ethan T. Neil, “Bayesian model averaging for analysis of lattice field theory results,” *Phys. Rev. D* **103**, 114502 (2021), [arXiv:2008.01069 \[stat.ME\]](#).
- [41] Colin Morningstar and Mike J. Peardon, “Analytic smearing of SU(3) link variables in lattice QCD,” *Phys. Rev. D* **69**, 054501 (2004), [arXiv:hep-lat/0311018](#).
- [42] Jülich Supercomputing Centre, “JUWELS Cluster and Booster: Exascale Pathfinder with Modular Supercomputing Architecture at Juelich Supercomputing Centre,” *Journal of large-scale research facilities* **7** (2021), 10.17815/jlsrf-7-183.
- [43] K. Jansen and C. Urbach, “tmLQCD: A Program suite to simulate Wilson Twisted mass Lattice QCD,” *Comput.Phys.Commun.* **180**, 2717–2738 (2009), [arXiv:0905.3331 \[hep-lat\]](#).
- [44] Abdou Abdel-Rehim, Florian Burger, Alber Deuzeman, Karl Jansen, Bartosz Kostrzewa, Luigi Scorzato, and Carsten Urbach, “Recent developments in the tmLQCD software suite,” *PoS LATTICE2013*, 414 (2014), [arXiv:1311.5495 \[hep-lat\]](#).
- [45] A. Deuzeman, K. Jansen, B. Kostrzewa, and C. Urbach, “Experiences with OpenMP in tmLQCD,” *PoS LATTICE2013*, 416 (2013), [arXiv:1311.4521 \[hep-lat\]](#).
- [46] Albert Deuzeman, Siebren Reker, and Carsten Urbach (ETM), “Lemon: an MPI parallel I/O library for data encapsulation using LIME,” *Comput. Phys. Commun.* **183**, 1321–1335 (2012), [arXiv:1106.4177 \[hep-lat\]](#).
- [47] M. A. Clark, R. Babich, K. Barros, R. C. Brower, and C. Rebbi, “Solving Lattice QCD systems of equations using mixed precision solvers on GPUs,” *Comput. Phys. Commun.* **181**, 1517–1528 (2010), [arXiv:0911.3191 \[hep-lat\]](#).
- [48] R. Babich, M. A. Clark, B. Joo, G. Shi, R. C. Brower, and S. Gottlieb, “Scaling Lattice QCD beyond 100 GPUs,” in *SC11 International Conference for High Performance Computing, Networking, Storage and Analysis Seattle, Washington, November 12-18, 2011* (2011) [arXiv:1109.2935 \[hep-lat\]](#).
- [49] M. A. Clark, Bálint Joó, Alexei Strelchenko, Michael Cheng, Arjun Gambhir, and Richard Brower, “Accel-

- erating Lattice QCD Multigrid on GPUs Using Fine-Grained Parallelization,” (2016), [arXiv:1612.07873](https://arxiv.org/abs/1612.07873) [hep-lat].
- [50] R Core Team, *R: A Language and Environment for Statistical Computing*, R Foundation for Statistical Computing, Vienna, Austria (2019).
- [51] M. Petschlies et al., “cvc package,” <https://github.com/marcuspetschlies/cvc> (2024).
- [52] Constantia Alexandrou, Martha Constantinou, and Haralambos Panagopoulos (ETM), “Renormalization functions for Nf=2 and Nf=4 twisted mass fermions,” *Phys. Rev. D* **95**, 034505 (2017), [arXiv:1509.00213](https://arxiv.org/abs/1509.00213) [hep-lat].
- [53] Sergio Caracciolo, Pietro Menotti, and Andrea Pelissetto, “One loop analytic computation of the energy momentum tensor for lattice gauge theories,” *Nucl. Phys. B* **375**, 195–239 (1992).
- [54] George Panagopoulos, Haralambos Panagopoulos, and Gregoris Spanoudes, “Two-loop renormalization and mixing of gluon and quark energy-momentum tensor operators,” *Phys. Rev. D* **103**, 014515 (2021), [arXiv:2010.02062](https://arxiv.org/abs/2010.02062) [hep-lat].
- [55] Constantia Alexandrou, Andreas Athenodorou, Krzysztof Cichy, Arthur Dromard, Elena Garcia-Ramos, Karl Jansen, Urs Wenger, and Falk Zimmermann, “Comparison of topological charge definitions in Lattice QCD,” *Eur. Phys. J. C* **80**, 424 (2020), [arXiv:1708.00696](https://arxiv.org/abs/1708.00696) [hep-lat].

I. SUPPLEMENTAL MATERIAL

A. Results for the bare and renormalized momentum fractions

The bare momentum fractions can be extracted from the ratios in Eq. (2) by performing a simultaneous fit for all $t_s > t_{s,\text{low}}$. In this way, from the set of all available t_s , $t_{s,\text{low}}$ marks the lowest value within this set from where we choose to fit. Figs. 5 and 6 show the overlay of the raw ratio data for individual source-sink separations t_s in the left-hand column and the fit for individual values of t_s in the center for the pion and the kaon, respectively, using the B ensemble as defined in Table I. Finally, the right-hand column shows the stability of the fit as we vary the lower bound $t_{s,\text{low}}$ of data sets included in the simultaneous fit. In Tables IV–VI we compile all the bare quantities extracted using this procedure for each ensemble. We show connected contributions as well as disconnected contributions and the component of the EMT used to extract those values for both the pion and the kaon.

In the case of the gluon contribution, we can perform two-state fits to the two- and three-point functions and compare them with the plateau fit results. In Fig. 7 we show the curves for the two-state fit and in Fig. 8 we show the comparison between the values extracted from the two-state fit and the plateau fit, and they are in agreement within errors. Because the errors increase very fast for the two-state fit, we decided to use only the plateau fit results in our analysis.

The renormalized results for the three ensembles are presented in Tables VII, VIII, and IX. The nominal difference of the renormalized results for the pion with our previous analysis on ensemble B (cB211.072.64) in Ref. [28] is rooted in the improvement of available statistics, especially for the gluon operator insertion, as well as the improvement in the determination of the renormalization and mixing coefficients.

In Fig. 9 we show the individual quark and gluon momentum fractions in the pion and kaon at the continuum limit using the numbers of Table II. The continuum limit has been calculated by fitting the results for each ensemble to a constant (including the three points and also the two points closer to the continuum) and the linear fit in a^2 . In Table III we present the result of these fits and the probabilities associated to each one.

B. Renormalization in the $\overline{\text{MS}}$ scheme

The bare quark and gluon average momentum fractions have been renormalized nonperturbatively by using the RI'/MOM scheme followed by perturbative conversion to $\overline{\text{MS}}$ at the scale $\mu = 2$ GeV. Based on global symmetries, the singlet quark and gluon EMTs in Eqs. (4 – 5) mix

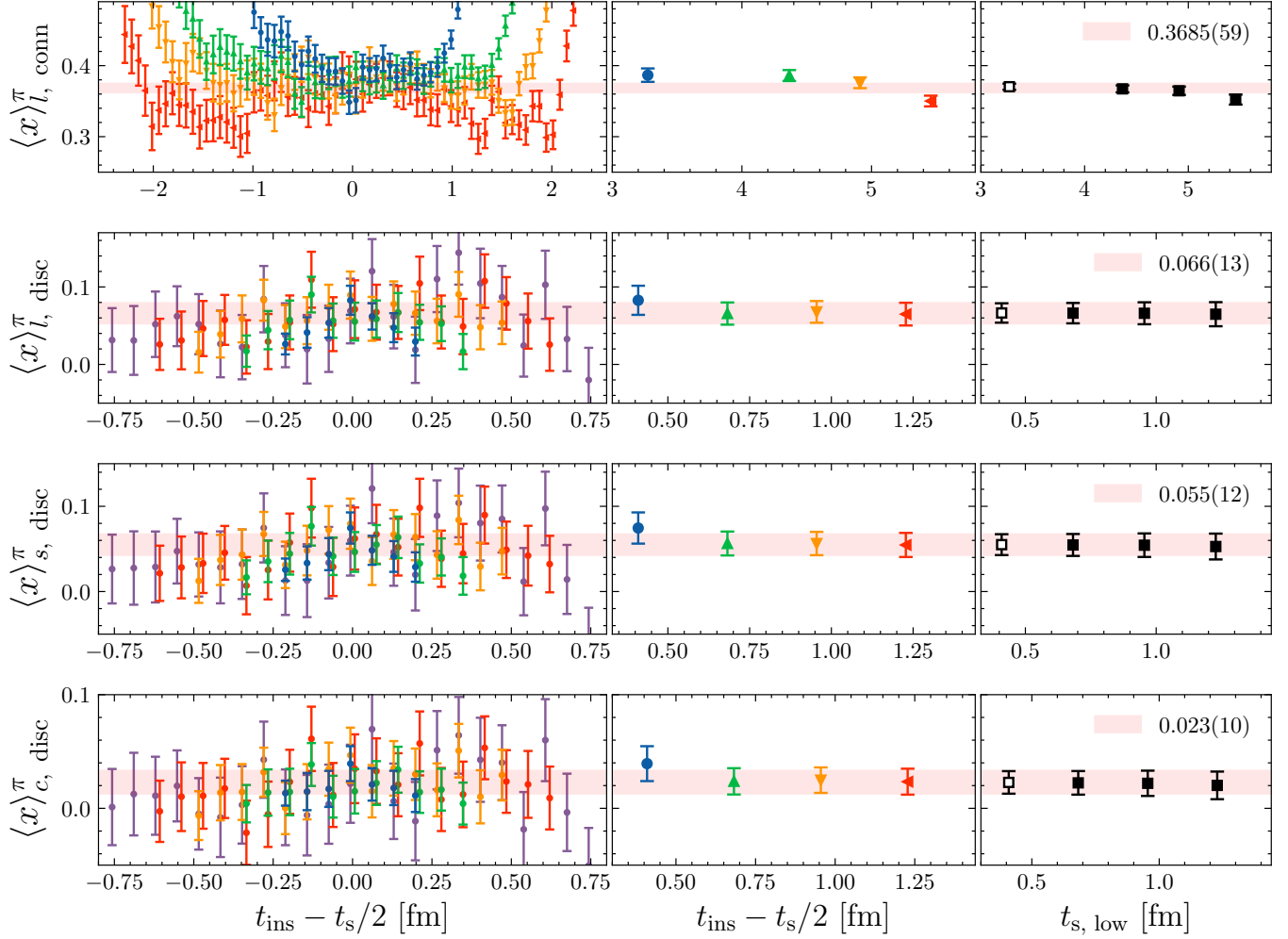


FIG. 5. Complete decomposition of the bare momentum fraction carried by quarks for the pion using the C ensemble. The two upper rows give the momentum fraction $\langle x \rangle_q$ carried by $u+d$ (top for connected and second row from top for disconnected), the 3rd row for the strange quark and the lower row for the charm quark. In the first column we show the bare ratio for different values of t_s , in the second column the individual fits per t_s , and in the last column the plateau fit as a function of the lowest value of t_s , $t_{s,\text{low}}$, used in the fits which demonstrates the convergence as a function of $t_{s,\text{low}}$ varies. The band shows the value after model averaging and the open symbol on the right panel corresponds to the fit with the highest probability.

TABLE III. Weights and values for each fit contributing to the continuum limit. Each row represents a different contribution to the momentum, from quarks or gluons, and then their sum for the pion and for the kaon. Each column represents the weight and value for each fit taken, with the first one the constant fit taking only two points, the second one the constant fit with three points and the last one the linear fit taking all three points.

	Plateau 2 points	Plateau 3 points	Linear fit
$\langle x \rangle_{q,R}^\pi$	0.218, 0.539(30)	0.523, 0.552(15)	0.259, 0.486(88)
$\langle x \rangle_{g,R}^\pi$	0.304, 0.403(35)	0.504, 0.375(21)	0.191, 0.398(94)
$\langle x \rangle_R^\pi$	0.237, 0.948(47)	0.555, 0.926(26)	0.208, 0.90(13)
$\langle x \rangle_{q,R}^K$	0.208, 0.609(18)	0.554, 0.612(10)	0.238, 0.642(55)
$\langle x \rangle_{g,R}^K$	0.317, 0.386(22)	0.296, 0.361(13)	0.387, 0.461(64)
$\langle x \rangle_R^K$	0.211, 0.998(28)	0.310, 0.973(17)	0.478, 1.115(85)

TABLE IV. Bare values for the different contributions for the B (cB211.072.64) ensemble.

Contribution	Operator	π	K
$\langle x \rangle_l^{\text{conn}}$	\bar{T}_{44}	0.3929(44)	0.1926(13)
$\langle x \rangle_s^{\text{conn}}$	\bar{T}_{44}	- - -	0.2694(06)
$\langle x \rangle_l^{\text{disc}}$	\bar{T}_{4k}	0.0612(59)	0.0510(34)
$\langle x \rangle_s^{\text{disc}}$	\bar{T}_{4k}	0.0441(58)	0.0385(32)
$\langle x \rangle_c^{\text{disc}}$	\bar{T}_{4k}	0.0150(46)	0.0137(23)

under renormalization according to Eq. (7). Due to the breaking of rotational symmetry on the lattice, $\bar{T}_{\mu=\nu}^{q(g)}$ and $\bar{T}_{\mu \neq \nu}^{q(g)}$ belong to different representations of the hypercubic group, and they are renormalized differently. The RI'/MOM renormalization matrix for each case is calculated by the following conditions:

$$\begin{pmatrix} Z_{qq}^{s,RI'} & Z_{gg}^{RI'} \\ Z_{qq}^{RI'} & Z_{gg}^{RI'} \end{pmatrix}^{-1} = \begin{pmatrix} \frac{1}{12} \text{Tr}[V_{qq}(V_{qq}^{\text{tree}})^{-1}] & V_{qq}(V_{gg}^{\text{tree}})^{-1} \\ \frac{1}{12} \text{Tr}[V_{gg}(V_{qq}^{\text{tree}})^{-1}] & V_{gg}(V_{gg}^{\text{tree}})^{-1} \end{pmatrix}, \quad (11)$$

where

$$V_{qq} = \frac{\langle q(p) \bar{T}_{\mu\nu}^q \bar{q}(p) \rangle_{\text{amp}}}{Z_{RI'}}, \quad (12)$$

$$V_{qq} = \frac{\langle \text{Tr}[A_\rho(p) A_\rho(-p)] \bar{T}_{\mu\nu}^q \rangle}{\langle \text{Tr}[A_\rho(p) A_\rho(-p)] \rangle}, \quad (13)$$

$$V_{gg} = \frac{\langle q(p) \bar{T}_{\mu\nu}^g \bar{q}(p) \rangle_{\text{amp}}}{Z_{RI'}}, \quad (14)$$

$$V_{gg} = \frac{\langle \text{Tr}[A_\rho(p) A_\rho(-p)] \bar{T}_{\mu\nu}^g \rangle}{\langle \text{Tr}[A_\rho(p) A_\rho(-p)] \rangle}, \quad (15)$$

and V_{qq}^{tree} (V_{gg}^{tree}) is the tree-level value of V_{qq} (V_{gg}). The renormalization factor of the quark field $Z_q^{RI'}$ is calculated in standard way through the quark propagator [52]. Note that in V_{gg} and V_{qq} , we set $\rho \neq (\mu, \nu)$ and $p_\rho = 0$ in order to cancel the mixing of EMTs with gauge-noninvariant operators [53], at least, to the leading order. For the same reason, in the case $\mu = \nu$, $\bar{T}_{\mu\nu}^{q(g)}$ is replaced by $\bar{T}_{\mu\mu}^{q(g)} - \bar{T}_{\sigma\sigma}^{q(g)}$, $\sigma \neq (\mu, \rho)$. The corresponding

TABLE V. Bare values for the different contributions to $\langle x \rangle$ for the C (cC211.060.80) ensemble.

Contribution	Operator	π	K
$\langle x \rangle_l^{\text{conn}}$	\bar{T}_{44}	0.369(06)	0.183(02)
$\langle x \rangle_s^{\text{conn}}$	\bar{T}_{44}	- - -	0.260(02)
$\langle x \rangle_l^{\text{disc}}$	\bar{T}_{4k}	0.066(13)	0.044(07)
$\langle x \rangle_s^{\text{disc}}$	\bar{T}_{4k}	0.055(12)	0.036(07)
$\langle x \rangle_c^{\text{disc}}$	\bar{T}_{4k}	0.023(10)	0.011(05)

TABLE VI. Bare values for the different contributions to $\langle x \rangle$ for the D (cD211.054.96) ensemble.

Contribution	Operator	π	K
$\langle x \rangle_l^{\text{conn}}$	\bar{T}_{44}	0.357(03)	0.180(02)
$\langle x \rangle_s^{\text{conn}}$	\bar{T}_{44}	- - -	0.249(01)
$\langle x \rangle_l^{\text{disc}}$	\bar{T}_{4k}	0.041(11)	0.055(07)
$\langle x \rangle_s^{\text{disc}}$	\bar{T}_{4k}	0.029(11)	0.047(07)
$\langle x \rangle_c^{\text{disc}}$	\bar{T}_{4k}	0.010(19)	0.045(11)

$\overline{\text{MS}}$ renormalization matrix is extracted through:

$$\begin{pmatrix} Z_{qq}^{s,\overline{\text{MS}}} & Z_{qq}^{\overline{\text{MS}}} \\ Z_{gg}^{\overline{\text{MS}}} & Z_{gg}^{\overline{\text{MS}}} \end{pmatrix}^{-1} = \begin{pmatrix} Z_{qq}^{s,RI'} & Z_{qq}^{RI'} \\ Z_{qq}^{RI'} & Z_{gg}^{RI'} \end{pmatrix}^{-1} \times \begin{pmatrix} C_{qq}^{\overline{\text{MS}},RI'} & C_{gg}^{\overline{\text{MS}},RI'} \\ C_{gg}^{\overline{\text{MS}},RI'} & C_{gg}^{\overline{\text{MS}},RI'} \end{pmatrix}^{-1}, \quad (16)$$

where $C_{ij}^{\overline{\text{MS}},RI'}$ are the conversion-matrix coefficients calculated up to two-loop order [54]. For the renormalization of flavor-nonsinglet combinations $\langle x \rangle_{u+d-2s}$ and $\langle x \rangle_{u+d+s-3c}$, the nonsinglet renormalization factor Z_{qq} is used, which is calculated from the connected part of V_{qq} (see [52]).

In this work, the diagonal elements $Z_{qq}^{s,\overline{\text{MS}}}$ and $Z_{gg}^{\overline{\text{MS}}}$ are evaluated non-perturbatively, while the off-diagonal $Z_{qq}^{\overline{\text{MS}}}$ and $Z_{gg}^{\overline{\text{MS}}}$ are calculated in one-loop lattice perturbation theory. For the non-perturbative calculations, we have employed high-statistical ($\sim 10000 - 30000$ configurations) $N_f = 4$ mass-degenerate ensembles generated by ETMC at the same lattice spacings of the three physical ensembles (see Table I). The parameters of the $N_f = 4$ ensembles are given in Table X.

An important aspect of our renormalization program is the improvement of the nonperturbative estimates by subtracting tree-level or one-loop discretization errors [52]. Stout smearing is employed in the gluon links of $\bar{T}_{\mu\nu}^g$ with the same set of smearing levels as used during the computation of the matrix elements for ensembles B, C and D. In the perturbative calculation of $Z_{qq}^{\overline{\text{MS}}}$, we restrict the stout smearing to three steps to manage the rapid growth of algebraic expressions, which can result in millions of terms when more stout-smearing steps are included. We have also employed Wilson flow (instead of stout smearing) in the nonperturbative calculations and we have confirmed the equivalence of the two smearing

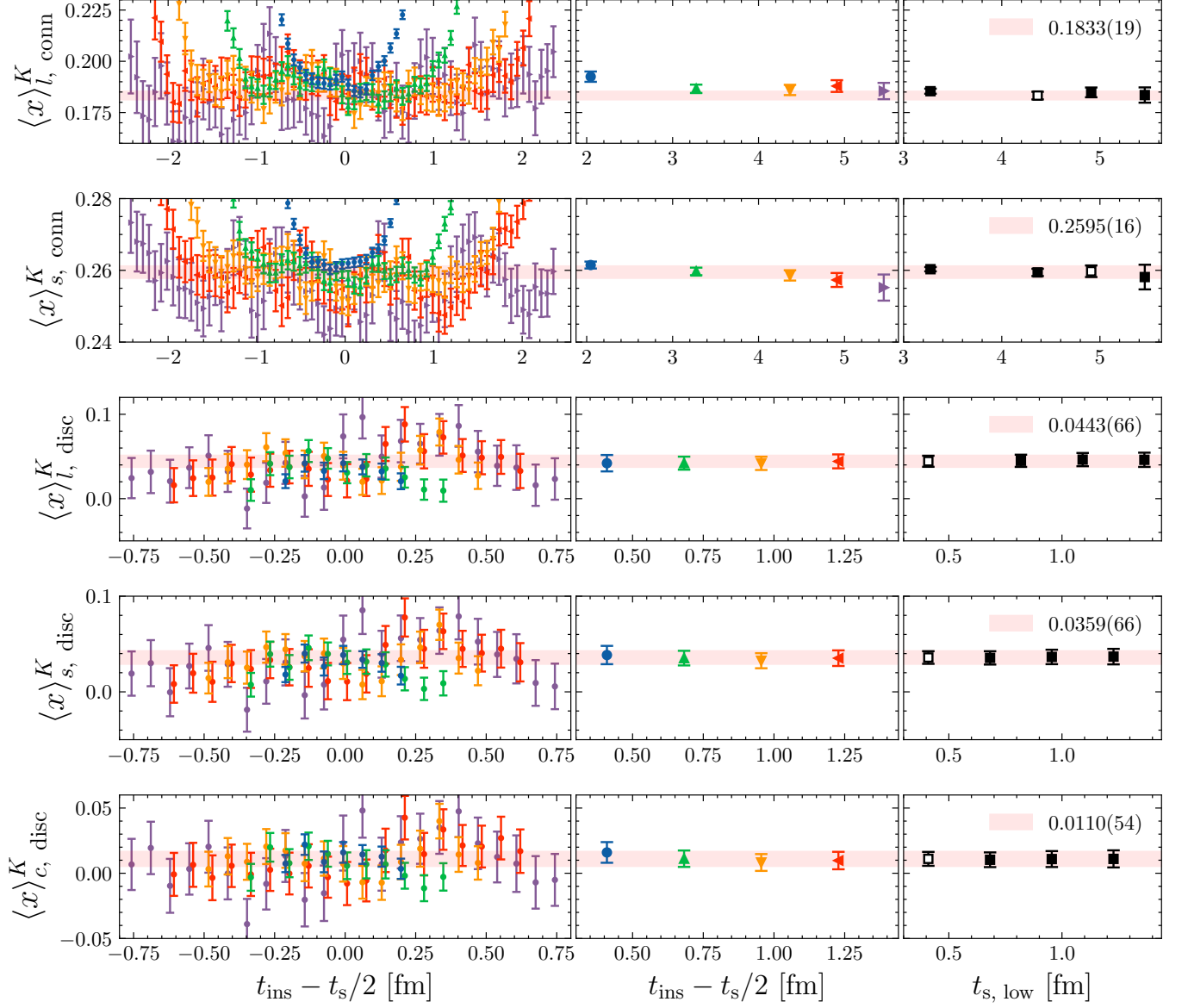


FIG. 6. Complete decomposition of the momentum carried by quarks in the kaon using the C ensemble. The notation is the same as that of Fig.5.

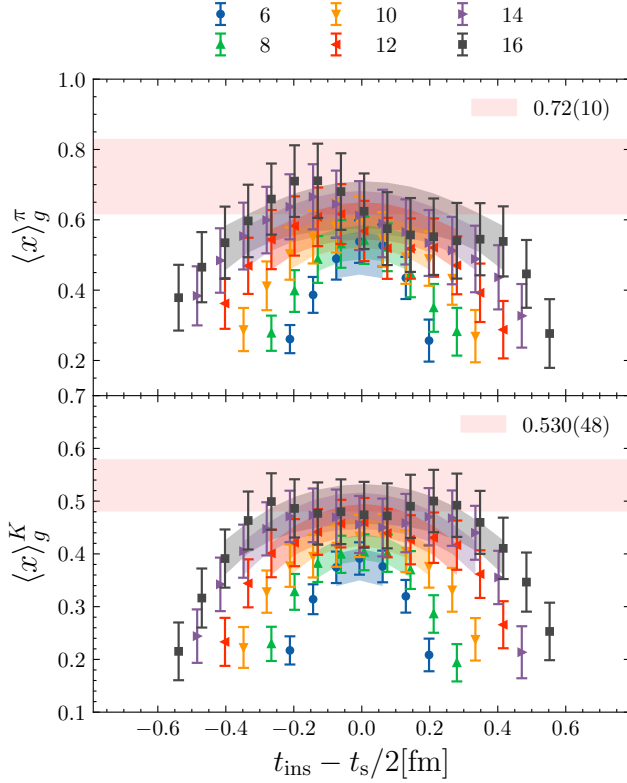


FIG. 7. Two state fit for both pion and kaon at 10 stout-smearing steps. The bands in colors are produced with the values of the fits to the correlators. The horizontal band shows the value after model averaging.

TABLE VII. Renormalized values for the different contributions for B (cB211.072.64) ensemble in the $\overline{\text{MS}}$ scheme at a scale of 2 GeV.

Contribution	π	K
$\langle x \rangle_{l,R}$	0.495(09)	0.264(05)
$\langle x \rangle_{s,R}$	0.047(07)	0.337(07)
$\langle x \rangle_{c,R}$	0.014(05)	0.013(03)
$\langle x \rangle_{q,R}$	0.557(18)	0.613(13)
$\langle x \rangle_{g,R}$	0.360(25)	0.346(16)

methods [55] when $\tau = \rho_{\text{stout}} N_{\text{stout}}$ (τ is the flow time, and $\rho_{\text{stout}}, N_{\text{stout}}$ are the stout parameter and number of stout-smearing steps, respectively). In table XI, we collect our results for the renormalization coefficients that enter our analysis.

C. Lattice setup

We provide additional information about the ETMC ensembles [39] in Tab. XII, together with volume of statistics used in this work.

The three different types of diagrams generated by the EMT insertions \bar{T}^q and \bar{T}^g into the pion and kaon cor-

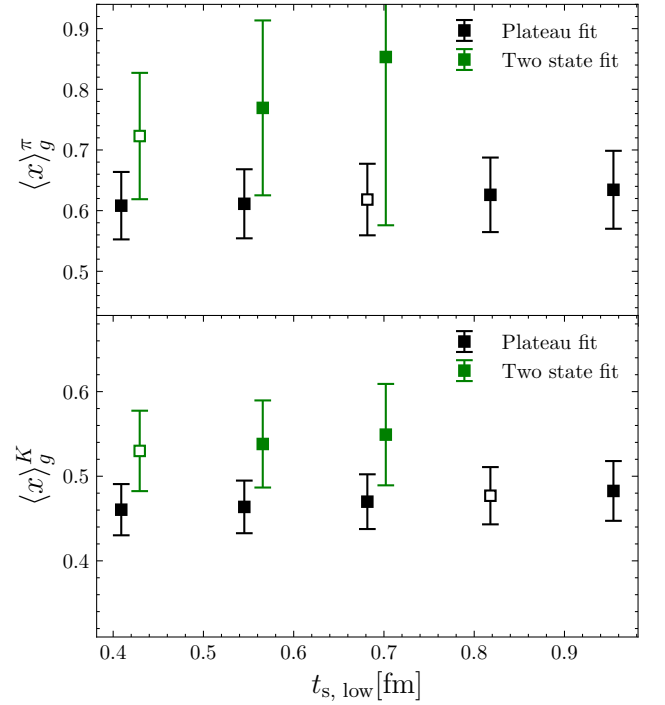


FIG. 8. Plateau and two-state fit for $\langle x \rangle_g$ for the pion (upper panel) and the kaon (lower panel). The black squares represent the values per $t_{s, \text{low}}$ for the plateau fit and the green squares the values for the two-state fit. Both fits agree, while the plateau shows a good stability at higher values of $t_{s, \text{low}}$ the two-state fit gains error faster. The open symbol shows the values with the highest probability for each fit.

TABLE VIII. Renormalized values for the different contributions for C (cC211.060.80) ensemble in the $\overline{\text{MS}}$ scheme at a scale of 2 GeV.

Contribution	π	K
$\langle x \rangle_{l,R}$	0.479(15)	0.249(08)
$\langle x \rangle_{s,R}$	0.059(14)	0.327(08)
$\langle x \rangle_{c,R}$	0.022(11)	0.009(06)
$\langle x \rangle_{q,R}$	0.560(38)	0.585(21)
$\langle x \rangle_{g,R}$	0.478(51)	0.375(28)

relation function are depicted in Fig. 10. We distinguish the (quark-)connected diagram (*I*), and the disconnected diagrams with a quark loop (*II*) from inserting \bar{T}^q and with the gluonic operator insertion \bar{T}^g in (*III*).

All quark-line (sub-)diagrams for three-point and two-point correlation functions are produced with stochastic timeslice-to-all propagators with randomly chosen source timeslices. In case of the connected three-point function diagram (*I*) we apply another sequential inversion through the hadron vertex at sink time.

To compute the diagrams involving strange or charm quark flow we use a mixed action for the strange and charm quark: to avoid the technical complication of strange and charm quark mixing inherent in the twisted mass sea quark action we introduce additional valence

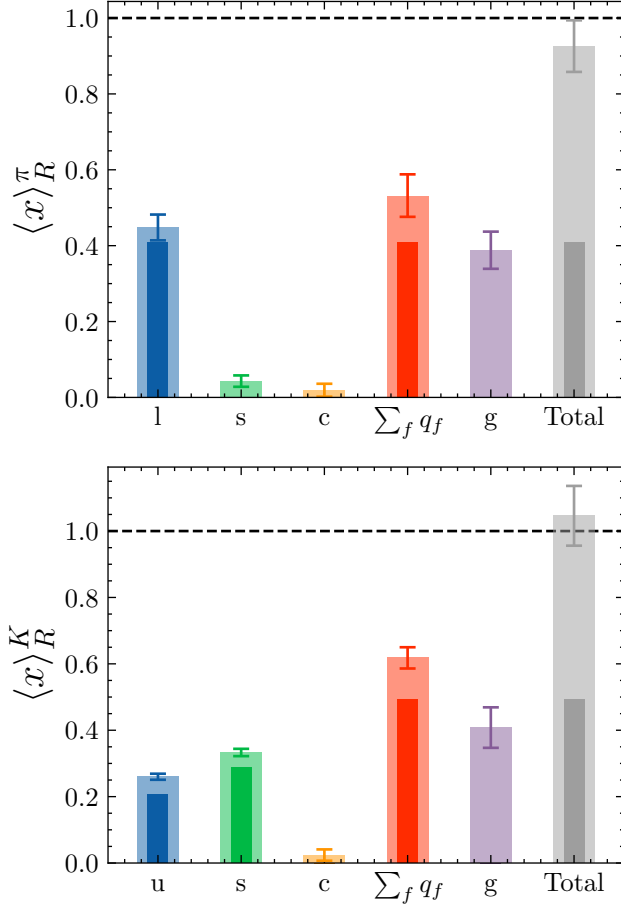


FIG. 9. The quark and gluon momentum fractions for the pion (upper panel) and kaon (lower panel) using the numbers in Table II. Inner bars represent only the connected contributions, while the outer bars show the total, including disconnected contributions.

TABLE IX. Renormalized values for the different contributions for D (cD211.054.96) ensemble in the $\overline{\text{MS}}$ scheme at a scale of 2 GeV.

Contribution	π	K
$\langle x \rangle_{l,R}$	0.459(15)	0.270(09)
$\langle x \rangle_{s,R}$	0.033(13)	0.342(12)
$\langle x \rangle_{c,R}$	0.012(22)	0.052(13)
$\langle x \rangle_{q,R}$	0.504(50)	0.664(32)
$\langle x \rangle_{g,R}$	0.337(48)	0.404(35)

TABLE X. $N_f = 4$ ensembles and their parameters used for the renormalization: $\beta = (2N/g^2)$, lattice volume ($L^3 \times T$), twisted-mass parameter ($a\mu$), hopping parameter κ and clover coefficient c_{SW} .

Ensemble					
Label	β	$L^3 \times T$	$a\mu$	κ	c_{SW}
B	1.778	$12^3 \times 24$	0.006	0.1393050	1.6900
C	1.836	$24^3 \times 48$	0.005	0.1386735	1.6452
D	1.900	$24^3 \times 48$	0.004	0.1379346	1.6112

TABLE XI. Renormalization coefficients in the $\overline{\text{MS}}$ scheme at 2 GeV for the three ensembles of Table X and for different tensor structures. For the computation of Z_{gg} , 5-10 steps of stout smearing are employed. The error quoted in the parenthesis is statistical; Z_{qq} and Z_{gq} have no statistical error because they are calculated in perturbation theory.

	Ensemble B	Ensemble C	Ensemble D
$Z_{qq}(\mu = \nu)$	1.0982(3)	1.1164(3)	1.1564(1)
$Z_{qq}(\mu \neq \nu)$	1.1228(2)	1.1481(3)	1.1825(1)
$Z_{qq}^s(\mu = \nu)$	1.0888(72)	1.0987(99)	1.1636(88)
$Z_{qq}^s(\mu \neq \nu)$	1.0996(15)	1.1323(12)	1.1740(12)
$Z_{gg}(\mu \neq \nu)$	-0.0106	-0.0145	-0.0188
$Z_{gq}(\mu = \nu)$	0.0658	0.0410	0.0139
$Z_{gq}(\mu \neq \nu)$	0.0772	0.0521	0.0246
$Z_{gg}^{n_{\text{st}}=5}(\mu \neq \nu)$	0.739(8)	0.727(21)	0.792(35)
$Z_{gg}^{n_{\text{st}}=6}(\mu \neq \nu)$	0.744(7)	0.738(19)	0.799(32)
$Z_{gg}^{n_{\text{st}}=7}(\mu \neq \nu)$	0.755(7)	0.753(18)	0.812(30)
$Z_{gg}^{n_{\text{st}}=8}(\mu \neq \nu)$	0.767(7)	0.769(17)	0.826(28)
$Z_{gg}^{n_{\text{st}}=9}(\mu \neq \nu)$	0.778(6)	0.784(16)	0.839(26)
$Z_{gg}^{n_{\text{st}}=10}(\mu \neq \nu)$	0.790(6)	0.797(16)	0.850(25)

TABLE XII. Statistics per ensemble used in this work. $n_{2\text{pt}}$ and $n_{3\text{pt}}$ give the number of stochastic samples produced per gauge configuration for two-point and (connected) three-point functions, respectively. In both cases stats is the total statistics for the given ensemble.

Label	Ensemble name	n_{conf}	$n_{2\text{pt}}$	stats	$n_{3\text{pt}}$	stats
B	cB211.072.64	755	400	302,000	8	6040
C	cC211.060.80	400	240	96,000	8	3200
D	cD211.054.96	499	600	299,400	8	3992

quark doublets for both strange and charm flavor in analogy to the light quark doublet with bare twisted masses of opposite sign within each doublet. These bare twisted valence quark masses, μ_s and μ_c , are tuned such that the Ω^- and Λ_c baryons take their physical values in the continuum limit, leading to the parameters given in Table XIII.

Observables derived from the mixed action retain automatic $\mathcal{O}(a)$ improvement with unitarity violations scaling equally at last at second order in the lattice spacing in the continuum limit.

Tables XII and XIV list the number of stochastic samples for two- and three-point functions per gauge configuration together with the total achieved statistics.

The quark loops for diagram (II) with covariant deriva-

TABLE XIII. The tuned strange μ_s and charm μ_c bare masses for the three ensembles

	B	C	D
$a\mu_s$	0.0186	0.01615	0.0136
$a\mu_c$	0.2490	0.2060	0.1660

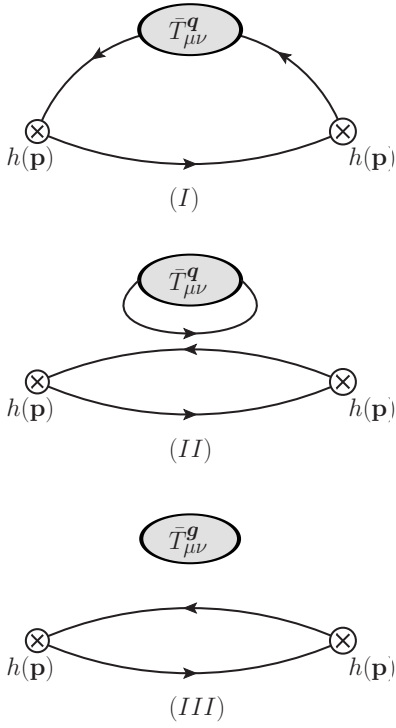


FIG. 10. Quark-flow diagrams for three-point function with quark and gluon energy momentum tensor operator insertion: (I) connected and (II) disconnected quark EMT insertion diagram, (III) disconnected gluon EMT insertion diagram.

TABLE XIV. For each quark flavor we give in this order the number of deflated low modes N_{defl} , the number of stochastic sources N_{srcs} and the probing distance N_{col} . We note that for the B and C ensembles, we have two sets of loops for the light quarks, which are averaged at the level of the analysis.

Ensemble	Light loops			Strange loops			Charm loops		
	N_{defl}	N_{srcs}	N_{col}	N_{defl}	N_{srcs}	N_{col}	N_{defl}	N_{srcs}	N_{col}
B	0	2	8	0	2	8	0	12	4
	200	1	8						
C	0	2	8	0	4	8	0	1	8
	450	1	8						
D	0	8	8	0	4	8	0	1	8

tive insertion are produced with hierarchical probing and full dilution in spin and color degrees of freedom. For the light quark loops of ensembles B and C additional data sets were produced using low-mode deflation on top of hierarchical probing. The parameters for the loop computation per gauge configuration are given in Table XIV.

For completeness we give the connection between the ratios of two- and three-point functions with EMT insertion \bar{T}^q , \bar{T}^g for tensor components used in this work and the bare $\langle x \rangle$ values in Eq. (17).

$$\begin{aligned}
 R_{44}^X(t_{\text{ins}}, t_s; \mathbf{0}) &\xrightarrow{t_s, t_{\text{ins}} \text{ large}} -\frac{3}{4} \langle x \rangle_X m_h, \\
 R_{4k}^X(t_{\text{ins}}, t_s; \mathbf{p}) &\xrightarrow{t_s, t_{\text{ins}} \text{ large}} \langle x \rangle_X p_k.
 \end{aligned}
 \tag{17}$$

In both cases the relation holds up to excited state contamination and up to the finite-time wrapping correction factor $[1 + \exp(-E_h(T - 2t_s))]^{-1}$ as given in Eq. (3).